AGU PUBLICATIONS

JGR

Journal of Geophysical Research: Space Physics

RESEARCH ARTICLE

10.1002/2014JA020356

Special Section:
Origins and Properties of Kappa Distributions

Observations in the *E* region ionosphere of kappa distribution functions associated with precipitating auroral electrons and discrete aurorae

S. R. Kaeppler[1], M. J. Nicolls[1], A. Strømme[1], C. A. Kletzing[2], and S. R. Bounds[2]

[1]SRI International, Menlo Park, California, USA, [2]Department of Physics and Astronomy, University of Iowa, Iowa City, Iowa, USA

Key Points:
- Kappa distribution functions characterize auroral electrons
- Observations of kappa distribution functions at *E* region altitudes
- Precipitating electrons exhibit a power law tail

Correspondence to:
S. R. Kaeppler,
stephen.kaeppler@sri.com

Citation:
Kaeppler, S. R., M. J. Nicolls, A. Strømme, C. A. Kletzing, and S. R. Bounds (2014), Observations in the *E* region ionosphere of kappa distribution functions associated with precipitating auroral electrons and discrete aurorae, *J. Geophys. Res. Space Physics*, *119*, 10,164–10,183, doi:10.1002/2014JA020356.

Received 1 JUL 2014
Accepted 20 OCT 2014
Accepted article online 26 OCT 2014
Published online 2 DEC 2014

Abstract Precipitating auroral electrons can produce discrete auroral arcs that contain signatures of the magnetospheric auroral source region. Differential number flux observations over two discrete aurorae were obtained by the Auroral Currents and Electrodynamics Structure sounding rocket mission, which successfully launched in 2009. These observations were made at *E* region altitudes of approximately 130 km. A model of precipitating auroral electrons as described by Evans (1974) was fit to the electron differential number flux obtained by the payloads, and parameters from the model were used to infer properties of the auroral source region. It is shown that the field-aligned precipitating electrons were better fit by a kappa distribution function versus a Maxwellian distribution function for the equatorward side of the first, quasi-stable, auroral arc crossing. The latter half of the first auroral arc crossing and second auroral crossing show that the precipitating electrons were better fit by a Maxwellian distribution function, which provides additional observational confirmation of previous studies. The low-energy electron population determined by the Evans (1974) model was within a factor of 2 of the observed differential number flux. The source region parameters determined from fitting the model to the data were compared with relevant studies from sounding rockets and satellites. Our observations are consistent with the results of Kletzing et al. (2003) that the plasma sheet electrons mapping to auroral zone invariant latitudes are characterized by kappa distribution functions.

1. Introduction

The electron spectrum associated with discrete aurora contains signatures of the mechanism that accelerates precipitating electrons and signatures of the electron distribution from the magnetospheric source. For the case of discrete aurora, it is well established that an electric field, parallel to the mean magnetic field, can accelerate precipitating auroral electrons to keV energies (see the recent review by *Karlsson* [2012, and references therein]). In some cases this parallel electric field is quasi-stable, which results in the electron spectra appearing as an inverted V signature [*Frank and Ackerson*, 1971; *Karlsson*, 2012, and references therein]. In other cases the electric field is time dependent, and the propagation of inertial Alfvén waves is one of the key mechanisms responsible for generating this time-dependent parallel electric field [*Goertz and Boswell*, 1979; *Kletzing*, 1994; *Stasiewicz et al.*, 2000]. Magnetic flux tubes connect regions within the plasma sheet to the auroral zone [*Winningham et al.*, 1975; *Feldshtein and Galperin*, 1985; *Newell et al.*, 1996; *Paschmann et al.*, 2002].

Evans [1974] examined the effect a parallel electric field would have on a Maxwellian source electron distribution while conserving the first adiabatic invariant. The parallel electric field accelerates electrons incident to it, causing a shift in energy of the differential number flux that would be observed by in situ measurements. One of the other consequences of the electrostatic potential drop is a "quasi-trapped" ionospheric population [*Albert and Lindstrom*, 1970], where electrons are trapped from above by the parallel electric field (for electrons that do not have enough parallel velocity to overcome the electrostatic potential drop) and from below by the magnetic mirror force. *Evans* [1974] showed that the results from this model were in very good agreement with precipitating electron flux results from the Injun 5 satellite. This method, which uses an accelerated Maxwellian distribution function to describe the precipitating auroral electron flux, has been applied to many observations by satellites and rockets [*Burch et al.*, 1976; *Winningham et al.*, 1977; *Pulliam et al.*, 1981; *Mallinckrodt*, 1985; *Reiff et al.*, 1988; *Shiokawa and Fukunishi*, 1991; *Shiokawa et al.*, 1990; *Olsson and Janhunen*, 1998; *Shiokawa et al.*, 2000]. However, very few studies have validated

the quasi-trapped electron flux predicted by the *Evans* [1974] model [*Winningham et al.*, 1977; *Pulliam et al.*, 1981].

A related formulation describing auroral electrons that are accelerated by a parallel electric field was derived by *Knight* [1973] and *Lemaire and Scherer* [1973, 1974]. The authors determined the magnitude of an electrostatic potential drop that was required to overcome the magnetic mirror force in order to carry current from the magnetosphere to the ionosphere. This current-voltage relation reduces to a linear form in the limit that $1 << \Phi_0/E_0 << B_0$, so that

$$j_{\parallel} \approx K\Phi_0 \tag{1}$$

where K is the "field-aligned conductance," Φ_0 is the magnitude of the electrostatic potential drop (in eV), E_0 is the source region electron temperature (in eV), and B_0 is the ratio of magnetic field strength at the ionosphere to the magnetic field strength at a location well above the potential drop [*Fridman and Lemaire*, 1980]. The current-voltage relation has been investigated theoretically [*Fridman and Lemaire*, 1980; *Janhunen and Olsson*, 1998; *Janhunen*, 1999]. It has been applied to the *Lyons* [1980] model of auroral electrodynamics, which coupled the magnetosphere and the ionosphere [*Lyons*, 1981; *Kletzing et al.*, 1996]. The current-voltage relation has been applied to sounding rocket data [*Lyons et al.*, 1979; *Bruening and Goertz*, 1986; *Shiokawa et al.*, 1990; *Kletzing et al.*, 1996], and many satellite observations, such as the Dynamics Explorer mission [*Weimer et al.*, 1987; *Lu et al.*, 1991], FREJA [*Olsson et al.*, 1998], Fast Auroral Snapshot Explorer [*Elphic et al.*, 1998], and Defense Meteorological Satellite Program (DMSP) [*Shiokawa and Fukunishi*, 1991; *Shiokawa et al.*, 2000].

Evans [1974] and *Knight* [1973] assumed that the source electron distribution was described by a Maxwellian distribution function. Satellite observations have suggested that the ion and electron populations in the plasma sheet exhibit behavior more consistent with a power law kappa distribution function, rather than a Maxwellian distribution function [*Vasyliunas*, 1968; *Christon et al.*, 1988, 1989, 1991; *Wing and Newell*, 1998; *Kletzing et al.*, 2003, and references therein]. *Olsson and Janhunen* [1998] fit the electron spectra of two events corresponding to a stable aurora and surging aurora using data from the FREJA satellite, at altitudes near 1750 km in the auroral zone, to examine the effect of the kappa distribution function on the field-aligned conductance (K in equation (1)). For the two events chosen, 18% of the spectra from the low-energy instrument (20 eV to 30 keV) were successfully fit. For the spectra fit by a kappa distribution, it was found that kappa fluctuated randomly between $\kappa = 4$ and 7. However, the kappa distribution had less than a 20% effect on the value of the field-aligned conductance versus the Maxwellian distribution; it was concluded that the tail of the kappa distribution did not significantly enhance the field-aligned conductance.

Kletzing et al. [2003] made one of the most complete surveys to date of the plasma sheet electron distribution using data from the HYDRA instrument on the Polar satellite. The Polar satellite measured the high-latitude plasma sheet at altitudes of 4.5–7 R_E and the HYDRA instrument had an energy range of 12 eV to 18 keV. The ionospheric foot points of the Polar satellite mapped to auroral invariant latitudes. In this statistical survey of 30,297 electron spectra, it was found that 45% of the electron spectra were successfully fit by a kappa distribution function ($\kappa \leq 10$) and 25% were successfully fit by a Maxwellian distribution function. Statistical averages were determined for properties of the poleward and equatorward edges; it was found that the equatorward side had, on average, higher electron number densities ($\langle n_e \rangle \approx 0.3\ \mathrm{cm}^{-3}$) and higher electron temperatures ($\langle E_0 \rangle \approx 900$ eV).

With respect to theoretical efforts, the current-voltage relationship was expanded to include kappa distribution functions [*Pierrard*, 1996; *Dors and Kletzing*, 1999; *Janhunen*, 1999]. *Dors and Kletzing* [1999] investigated the consequences of including a kappa distribution in the *Lyons* [1980] model of auroral electrodynamics. However, this investigation was theoretical only and not compared with observational data.

Ogasawara et al. [2006] is one of few studies that has reported observations of kappa distributions associated with auroral electrons at *E* region altitudes. A sounding rocket payload flew through two arcs, with midpoint altitudes of 110 km and 125 km, respectively. The payload was instrumented with solid state electron detectors with an energy range of 3.5–65 keV, thus sampling the higher-energy portion of the precipitating electron spectra. One of the limitations of these detectors was their orientation relative to the mean magnetic field, which resulted in pitch angle coverage from 70 to 110°, primarily perpendicular to the

mean magnetic field. It was found that the precipitating electron spectra near and within the auroral arc were fit by a kappa distribution with κ =5–8 and temperatures between 100 and 720 eV.

In this paper, observations from the Auroral Currents and Electrodynamics Structure (ACES) sounding rocket mission are examined to determine if signatures in the electron spectra are consistent with a kappa distribution function. We develop a model which quantifies the effect a parallel electric field has on accelerating an electron distribution function. This model also includes the quasi-trapped electron population. The ACES payloads traversed two discrete aurorae, which are discussed in the following section. The in situ differential number flux that corresponds to traversing these two arcs were fit to the model, and we infer properties of the auroral source region from the model parameters. A Monte Carlo analysis is undertaken to quantify the uncertainty on the parameter estimates based on the uncertainties in the in situ data. The parameters characterizing the source region electron distribution are discussed within the context of relevant previous satellite and sounding rocket studies.

2. The ACES Sounding Rocket Mission

The ACES sounding rocket mission was devised to make multipoint observations to probe the current structure, electrodynamics, and energy transfer of a discrete auroral arc system. Two payloads were flown. A high-altitude payload (hereafter referred to as "ACES High") measured the input electrodynamic and plasma parameters into the region in the auroral ionosphere where currents close. A low-altitude payload (hereafter referred to as "ACES Low") made in situ observations of plasma parameters and electrodynamics within the *E* region ionosphere. Both payloads crossed similar magnetic flux tubes nearly simultaneously to constrain the spatial-temporal ambiguity inherent to in situ observations.

ACES High and Low successfully launched from the Poker Flat Research Range, Alaska, on 29 January 2009 at 09:49:40.0 UT and 09:51:10.0 UT, respectively. The overall geomagnetic conditions preceding the launch were very quiet because the launch window was near the 2009 solar minimum. However, the payloads were launched into a dynamic multiple-arc aurora located north of Fort Yukon, Alaska, the approximate apogee location of both payloads. The ground-based magnetometers indicated a 100 nT deflection in the *H* component observed at Fort Yukon. The launch was at approximately 23:00 MLT, which was near the midnight MLT sector.

The electron detectors flown on both payloads were top hat style electrostatic analyzers that stepped in energy from 10 eV to 16 keV in 47 logarithmic steps, producing full pitch angle distributions from 0° to 180°, which were binned in 15° increments. The electron detectors on ACES Low performed nominally. However, the ACES Low payload suffered from a failure in the attitude control system: a gas valve remained open, causing the payload to be misaligned with the mean magnetic field. This motion resulted in a lack of coverage of the differential number flux measurements, primarily at the pitch angle bin centered at 0°. A detailed description of the ACES mission setup, instrumentation, data, and results from these payloads can be found in *Kaeppler et al.* [2012].

Kaeppler et al. [2012] identified two auroral arc crossings that were traversed by both of the ACES payloads: a "quasi-stable" arc crossing and a "westward moving" auroral region. Figure 1, a montage using the Time History of Events and Macroscale Interactions during Substorms (THEMIS) all-sky imager at Fort Yukon, Alaska shows the evolution of the auroral event, particularly focusing on the passage of the ACES Low payload through the quasi-stable arc and the westward moving aurora. The cardinal directions are shown in magnetic coordinates by the dashed line as magnetic North and East; ACES High and Low are represented by the "H" and "L." Figure 1a shows ACES Low as it entered into the quasi-stable arc at 09:54:06 UT, approximately 40 s after ACES High [*Kaeppler et al.*, 2012]. This quasi-stable arc had moved equatorward when ACES High entered the arc, yet remained spatially stable in the zonal direction during the passage of ACES Low. The visible intensity of the arc began to fade significantly after 09:54:15 UT, which is the time interval shown in Figure 1b. ACES Low exited the visible portion of the quasi-stable arc at approximately 09:54:28 UT. Figures 1b and 1c show that the westward moving auroral region in the center of the frames is rotating and moving slowly westward. ACES Low entered a faint auroral extension from the westward edge of the westward moving auroral region, and the payload continued to traverse through the westward moving and circulating region until 09:55:15 UT. Figure 1d shows that ACES Low may still be traversing through a weak visible extension of the faint remnant of the westward moving auroral region.

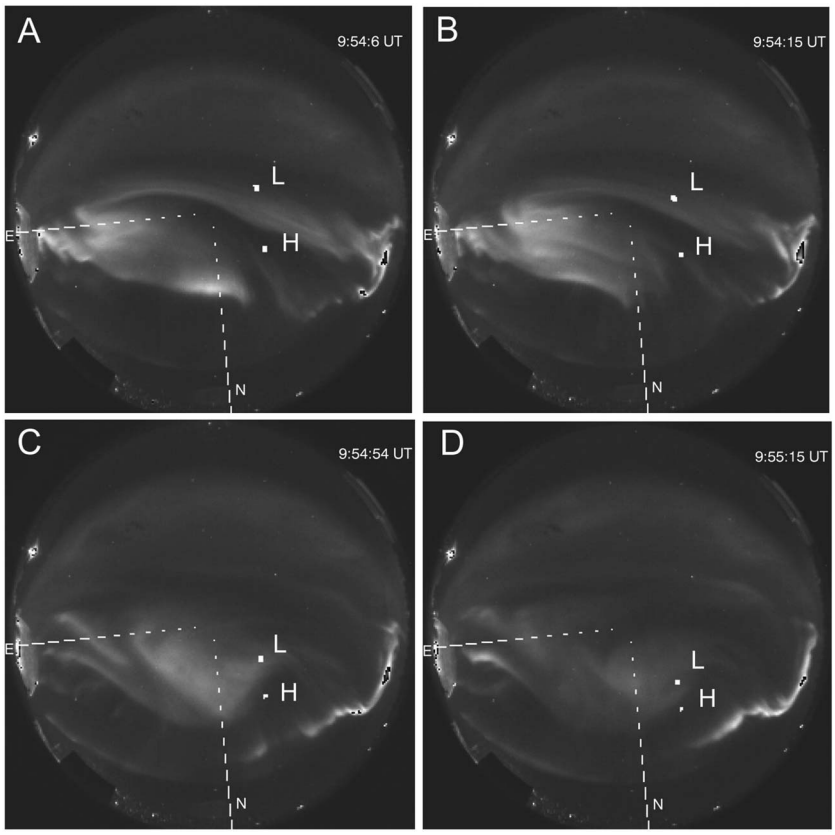

Figure 1. (a–d) Time History of Events and Macroscale Interactions during Substorms (THEMIS) Fort Yukon all-sky imager data of the auroral event that was traversed by ACES High (H) and ACES Low (L).

3. Auroral Particle Precipitation Model

3.1. Model Description

A model of the type described by *Evans* [1974] was chosen to characterize the auroral electron spectra and infer properties of the source electron distribution at ionospheric altitudes. This model includes both the component of precipitating electrons that have been accelerated by a parallel electric field at an altitude of 1–2 R_e (geocentric 2–3 R_e) [*Bennett et al.*, 1983; *Borovsky*, 1993; *Karlsson*, 2012, and references therein], and the quasi-trapped ionospheric electrons. The motivation for modeling the electron flux is to parameterize the precipitating electron flux in terms of the source electron distribution that is assumed to be isotropic as it passed into a parallel electrostatic potential drop. The figure of merit is to determine how well the model can reproduce the data observed by the ACES Low payload at a given pitch angle and what the resulting parameter estimates imply about the source electron distribution.

To describe the acceleration of precipitating electrons, the Evans model assumes that an infinitely thin electrostatic potential drop is located on a magnetic flux tube. The location of the source region is determined by the parameter B_0, which is the ratio of the magnetic field strength at the ionosphere to the magnetic field strength at the location of the electrostatic potential drop,

$$B_0 = B_I/B_A \approx \left(\frac{R_e + z_I}{R_e + z_A}\right)^3 \tag{2}$$

where z_I corresponds to the altitude of the ionospheric foot point (ACES Low location), and z_A is the altitude at the top (magnetospheric side) of the potential drop [*Bruening and Goertz*, 1986]. The parallel velocity component gains the energy of the acceleration by the parallel electric field. The first adiabatic invariant is conserved along the magnetic flux tube, including through the electrostatic potential drop. For simplicity, it is assumed that the effects of heating within the acceleration region are negligible [*Reiff et al.*, 1988; *Shiokawa et al.*, 1990, 2000] and the effects of an extended potential structure along the magnetic field line

are also neglected. This is justifiable because the altitude of the ACES payload is nearly at the foot point of the magnetic flux tube, well below the altitude z_A. The focus of this study is on the resulting electron flux after acceleration by a parallel electric field, not necessarily what mechanism(s) are causing the parallel electric field; this question is not investigated further in this study.

The electron flux was determined at ACES Low altitudes by applying Liouville's theorem, which maps regions in phase space, provided there are no collisions [*Dors and Kletzing*, 1999; *Wing and Newell*, 1998]. A grid in velocity space was created at the altitude of ACES Low and the velocity components were mapped up to the top (magnetospheric side) of the electrostatic potential drop, which is set by the value of B_0. To good approximation, collisions along the flux tube are negligible, so by Liouville's theorem, $f_A(v_\parallel, v_\perp) = f_I(v_\parallel, v_\perp)$, where A corresponds to the topside of the potential drop and I corresponds to the ionosphere. The differential number flux was computed numerically on the velocity grid, as a function of pitch angle and energy, using the relation from *Baumjohann and Treumann* [1996].

$$J(E, \alpha) = \frac{2E}{m_e^2} f_I(v_\parallel, v_\perp) \tag{3}$$

The electron flux below the energy of the electrostatic potential drop contains two populations: degraded primary electrons and electrons of ionospheric origin [*Chiu and Schulz*, 1978]. The accelerated auroral electrons interact with the ionospheric neutrals through ionization (secondary electrons) and scattering (degraded primaries). These interactions create the quasi-trapped population. The magnitude of the quasi-trapped flux was determined using the magnitude of the accelerated electron flux, and the ionospheric response shown in Figures 2 and 3 in *Evans* [1974], which were originally derived from the model by *Banks et al.* [1974]. Secondary and degraded primary electrons, generated from accelerated electrons, are assumed to be isotropic and moving upward (toward the magnetosphere); these electrons will precipitate back onto the ionosphere if the velocity component parallel to the mean magnetic field is not large enough to overcome the high-altitude electrostatic potential drop. This impinging precipitation, composed of secondary electrons and degraded primaries, generates tertiary ionospheric electron flux. If the tertiary electron flux does not overcome the electrostatic potential drop, it will again precipitate back onto the ionosphere, generating additional electron flux. The additional flux created continues to diminish on additional iterations or "bounces," so that a steady state is attained. This steady state process is described in Figure 8 of *Pulliam et al.* [1981].

The ionospheric flux from the backscatter (degraded primaries) and secondary (ionization) electrons were determined independently. For our model, it was found that a steady state configuration was reached after four iterations ("bounces"), which is consistent with the number of iterations used by *Pulliam et al.* [1981]. Additional iterations were found to contribute negligibly to the upward component of the electron flux.

The flux produced from the quasi-trapped ionospheric contribution was assumed to be isotropic *Evans* [1974]. A fraction of the quasi-trapped contribution has energies larger than the magnitude of the electrostatic potential drop and would have enough energy to escape into the magnetosphere. To account for this loss, the following relation was applied to the isotropic upward flux, Φ_{up},

$$G(E) = \begin{cases} 1 & \text{for } E < \Phi_0 \\ 1 - B_0\left(1 - \Phi_0/E\right) & \text{for } \Phi_0 \le E \le \Phi_0\left(\frac{B_0}{B_0 - 1}\right) \\ 0 & \text{for } E > \Phi_0\left(\frac{B_0}{B_0 - 1}\right) \end{cases} \tag{4}$$

where Φ_0 corresponds to the magnitude of the electrostatic potential drop, E is the energy grid for the differential number flux, and B_0 is defined in equation (2). This loss term accounts for the sharp dip in the differential number flux that is seen in the 45° pitch angle case in Figure 5b of *Evans* [1974].

Once the equilibrium electron flux from both the precipitating portion and the ionospheric quasi-trapped portion is determined, it is numerically integrated over pitch angle to determine the parallel differential number flux, $\Phi_\parallel(E)$, or if integrated over energy and pitch angle, the total number parallel flux $\Phi_\parallel$. For this study, the differential and total number flux correspond to the flux passing parallel through a unit surface, rather than the flux passing through a unit sphere. Additional details on how the auroral precipitation model was developed can be found in *Kaeppler* [2013].

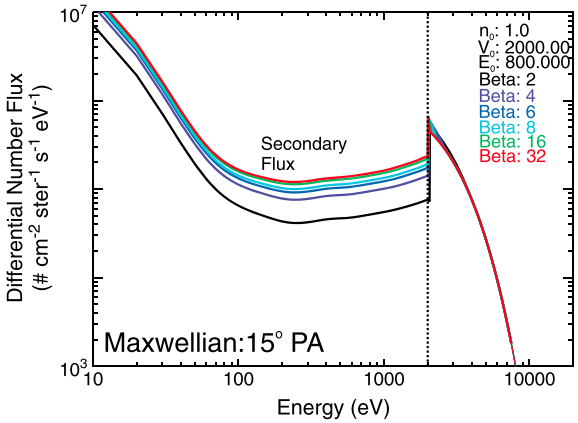

Figure 2. The quasi-trapped and accelerated electron flux as a function of the parameter B_0, holding the other parameters fixed. Increasing the value of B_0 has a diminishing increase on the magnitude of the trapped electron flux at energies below the magnitude of the electrostatic potential drop.

The source electron distribution at the top of the potential drop remains the key term to be specified for this model. As discussed in section 1, the Maxwellian distribution has been used extensively in past studies to describe the electrons. However, more recent observations have suggested that the auroral source region may be better described by a kappa distribution function [*Kletzing et al.*, 2003; *Olsson and Janhunen*, 1998]. The electron distribution functions we model are described by five parameters: n_0, the electron number density at the top of the potential drop; E_0, the temperature of the distribution (in eV); Φ_0, the magnitude of the electrostatic potential drop (in eV) which the electrons fall through; the index κ; and B_0. Following the definition of the kappa distribution from *Baumjohann and Treumann* [1996] at the top of the potential drop,

$$f_\kappa(E) = n\left(\frac{m_e}{2\pi\kappa E_\kappa}\right)^{3/2}\frac{\Gamma(\kappa+1)}{\Gamma(\kappa-1/2)}\left[1+\frac{E}{\kappa E_\kappa}\right]^{-(\kappa+1)} \tag{5}$$

where

$$E_\kappa = E_0(1-3/2\kappa) \tag{6}$$

is the most probable energy in units of eV [*Baumjohann and Treumann*, 1996]. The energy (E) used in equation (5) is a function of the potential drop Φ_0 and B_0 since the parallel and perpendicular velocity components are mapped from the ionosphere to the top of the potential drop. To be consistent with Liouville's theorem and the steady state assumption, the parameters do not vary along the magnetic flux tube connecting the top of the electrostatic potential drop to the ionospheric foot point.

The kappa distribution has a few advantages. First, it is effectively a generalization of a Maxwellian with a power law tail. Thus, the kappa distribution is a convenient way to incorporating in a power law tail. It can be demonstrated in the limit that $\kappa \to \infty$, the kappa distribution asymptotes to a Maxwellian distribution. For the energy range of the electrons measured by ACES Low, a value of $\kappa \geq 10$ is effectively the same as a Maxwellian distribution. The second advantage comes from fitting the source distribution; the kappa distribution has four free parameters (n_0, Φ_0, E_κ, and κ), whereas the Maxwellian distribution has only three parameters (n_0, Φ_0, and E_0). B_0 is fixed in both cases.

3.2. Parameter Estimation

The Levenberg-Marquardt least squares fitting routine [*Press et al.*, 2007] was used to fit this model to the differential number flux observed on ACES Low. One limitation in using the Levenberg-Marquardt (hereafter referred to as "LM") routine is that it produces a local rather than global solution in parameter space. This motivates a careful determination of initial "guess" parameter estimates, which will be discussed in the remainder of this section.

The value of B_0 was fixed for the parameter estimation; this was done for three reasons. First, the magnetic field ratio controls the transfer of parallel velocity into the perpendicular component to conserve the first adiabatic invariant. For ACES Low, the field-aligned flux extended out to the pitch angle centered at 30° for both of the arc crossings, which is consistent with the value of B_0 that was chosen. The second factor is that B_0 controls the magnitude of the trapped degraded primary and secondary electrons. Figure 2 shows the effect of increasing the value of B_0 while holding the other parameters fixed. There is less than a factor of 2 difference between $B_0 = 6$ and 32. This result leads to the third point: there is not a strong dependence upon the parameter B_0, especially as it becomes very large. One of the consequences of $1 << \Phi_0/E_0 << B_0$ is that B_0 effectively vanishes from the current-voltage relation, so that the current-voltage relation reverts

to its linear form, equation (1). The value of B_0 for this study was fixed at 6, since it produces spread in the electron flux to 30° pitch angle yet corresponds to a potential drop located at an altitude of approximately 0.8 R_e (≈ 5000 km).

The two parameters that are most difficult to constrain properly are the electron number density n_0 at the top of the potential drop and the magnitude of the electrostatic potential drop Φ_0. As can be seen in equation (1), an increase (decrease) in the source electron density corresponds to a decrease (increase) in the potential drop magnitude when the total parallel number flux remains constant. This suggests that combinations of n_0 or Φ_0 can produce very similar differential number fluxes. However, the combination of n_0 and Φ_0 chosen must be consistent with the data that were observed.

A routine was developed to determine the magnitude of Φ_0 based on an estimate of the peak differential number flux observed by ACES Low. The definition of peak flux in this case does not mean the maximum value of the flux observed over the full energy range of the electron detectors; rather, it is the maximum value of the flux immediately preceding the exponential or power law decay in the electron spectrum. The energy corresponding to this maximum flux value is the magnitude of the potential drop, Φ_0, at 0° pitch angle [*Evans*, 1974]. There is some uncertainty in determining Φ_0 in this way because of the logarithmic step in the energy sweep for the electron detector, which had a step value of approximately 400 eV, for E >1000 eV. It was found that setting Φ_0 to be the preceding energy step (and allowing the fitting routine to adjust Φ_0 for the best fit) of the electron detector sweep as the initial guess produced lower values of reduced χ^2 in the LM routine (hereafter reduced χ^2 will be represented as χ^2_ν, following the convention of *Bevington and Robinson* [2003]).

The estimate of Φ_0 at the peak flux and the current-voltage relation were used to obtain an initial guess for n_0. *Pierrard* [1996] and *Dors and Kletzing* [1999] modified the current-voltage relation for kappa distribution function, where the parallel number flux observed at the ACES Low location is

$$\Phi_\parallel^L = A_\kappa - A_\kappa\left(1 - \frac{1}{B_0}\right)\left[1 + \frac{\Phi_0}{E_0(\kappa - \frac{3}{2})(B_0 - 1)}\right]^{-\kappa+1} \tag{7}$$

where

$$A_\kappa = \frac{n_0 B_0}{2}\left(\frac{E_0(2\kappa - 3)}{\pi m_e}\right)^{1/2}\left[\frac{\Gamma(\kappa + 1)}{\kappa(\kappa - 1)\Gamma(\kappa - \frac{1}{2})}\right] \tag{8}$$

and has units of $cm^{-2}\ s^{-1}$. The L corresponds to the precipitating number flux for the ACES Low payload. An estimate of the total parallel number flux was obtained from the in situ measurements by integrating over energy and pitch angle,

$$\Phi_\parallel^L = \int_0^{90} \cos(\alpha)\sin(\alpha)\,d\alpha \int_{\Phi_0}^{16\,\mathrm{keV}} J(E,\alpha)\,dE \tag{9}$$

where α corresponds to pitch angle, 16 keV is the maximum energy of the electron detectors on ACES Low, and $J(E, \alpha)$ is the observed differential number flux at a given pitch angle. The parameter n_0 can be determined from equation (7) using the estimated value for Φ_0, the total number flux determined by numerically integrating equation (9), and some estimates for E_0, κ, and B_0. The estimate of Φ_0 is the critical parameter in the integration of the total parallel number flux, since the portion of the distribution function being integrated over corresponds to energies above the magnitude of the potential drop.

As was suggested in *Wing and Newell* [1998], it may be difficult to distinguish between Maxwellian distribution functions and kappa distribution functions for $\kappa \geq 10$, considering that the energy range of the electron detectors used on ACES was similar to that used on DMSP satellites. For our purposes, κ is initially set to 10, which is consistent with an effective Maxwellian distribution function, and fitting routine determines whether the kappa distribution is a better fit to the data.

4. Results

The in situ data were fit over two time intervals corresponding to the quasi-stable auroral arc crossing and the westward moving auroral crossing, as shown in Figure 1. The electron spectra for the pitch angle bins

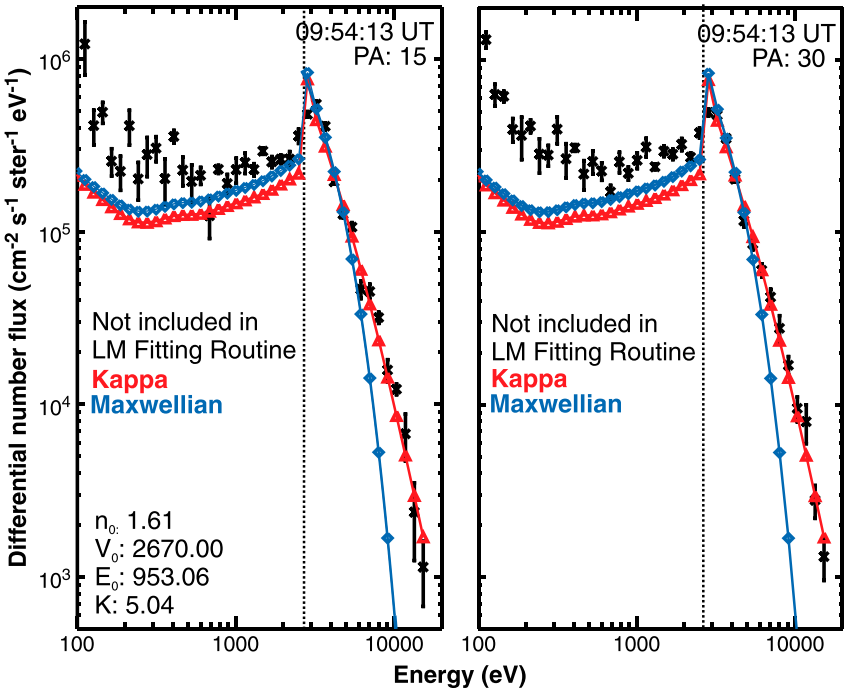

Figure 3. An example of the differential number flux for the pitch angle bins centered at (left) 15° and (right) 30°. The differential number flux observed by the electron detectors is shown in black, including errors. The solid red line and the triangles are the differential number flux of the kappa distribution function using parameters from the fitting routine and including the quasi-trapped flux. The solid blue line with the diamond shows the differential number flux using parameters from the fitting routine for a Maxwellian distribution function. For energies greater than the vertical dotted black line, those data were included in the LM fitting routine; for energies less than that line, those data were not included in the fitting routine. For this instance, the kappa distribution is a superior fit to the observed data.

centered at 15° and 30° were averaged over five data time intervals to obtain the mean and standard deviation (σ), respectively. The electron spectra from both pitch angles were fit simultaneously, and the standard error ($\sigma/\sqrt{5}$) was used as an estimate of uncertainty [*Bevington and Robinson*, 2003]. The highest time resolution of the electron flux data is 48 ms, corresponding to an energy sweep, so averaging over five data intervals creates a mean spectrum covering approximately 192 ms.

An example of a model instance is shown in Figure 3 for the pitch angle bins centered at 15° (left) and 30° (right). Figure 3 (left) shows the differential number flux at the time 09:54:13 UT, which was within the quasi-stable arc, plotted as a function of energy. Energies below 100 eV were not included. The observations from the ACES Low electron detector are shown as black crosses, along with their corresponding error bars. The red line with triangles is the model instance using the fit parameter estimates and also includes the quasi-trapped population at energies below the magnitude of the electrostatic potential drop (in this case, $\Phi_0 \approx 2700$ eV). We emphasize that the data below the magnitude of the potential drop are not used in the fitting routine. The parameter estimates for the fit are listed in the lower left corner of Figure 3 (left). The blue curve with diamonds is the model instance using a Maxwellian distribution function; it includes the quasi-trapped ionospheric contribution. Figure 3 (right) for the 30° pitch angle bin is in a similar format.

The power law tail of the kappa distribution is clearly a better fit with the in situ electron flux for both pitch angle bins in Figure 3. The energy channels near the peak flux produce similar differential number flux values for the Maxwellian and kappa distributions, but the shape of the power law decay ($\kappa \approx 5$) is a better fit with the observed differential number flux measurements. The discontinuity that separates the accelerated electron flux from the quasi-trapped flux near the electrostatic potential drop, Φ_0, is an artifact of the model by *Evans* [1974]. There is not a smooth description between the quasi-trapped and the accelerated portion of the electron flux. Previous studies that have applied the model by *Evans* [1974] show that the observed data and the model results are in good agreement, except near the discontinuity, where the data from the

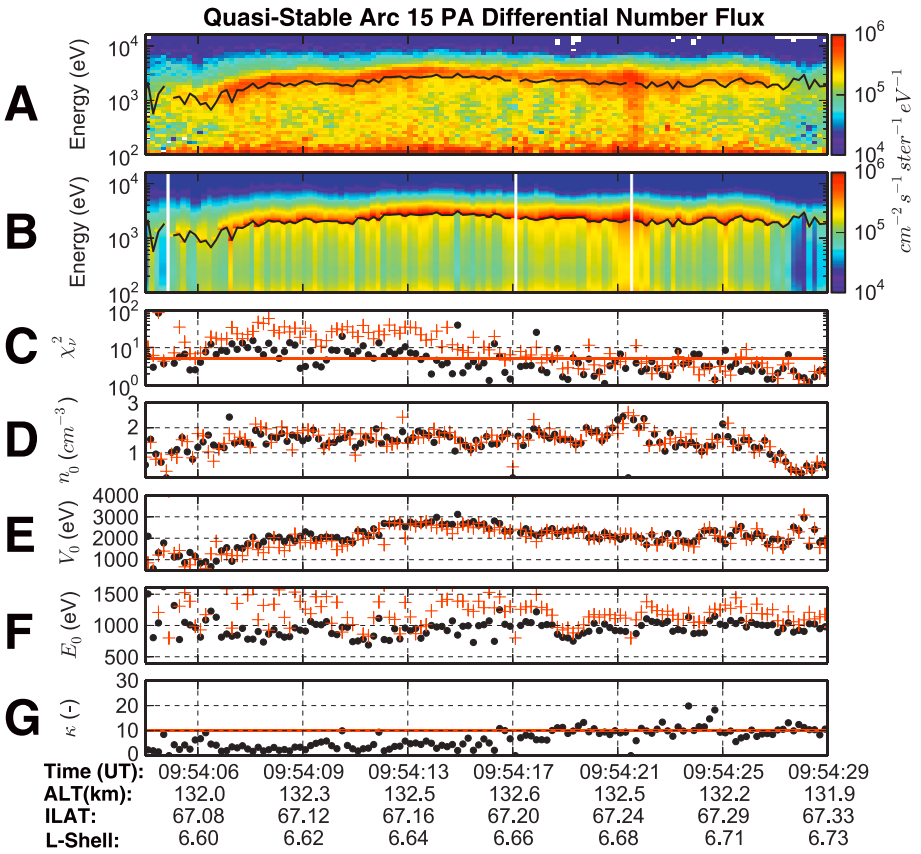

Figure 4. Data are presented for the first quasi-stable auroral arc crossing. (a) Differential number flux observed by the ACES payload for the pitch angle centered at 15°. (b) The differential number flux for the pitch angle centered at 15° using the kappa distribution. (c) Reduced χ^2. (d) Source electron density, n_0. (e) Electrostatic potential drop, Φ_0. (f) Source electron temperature, E_κ. (g) The κ parameter. Black dots correspond to parameter estimates using a kappa distribution, and red crosses correspond to parameter estimates using a Maxwellian distribution. The black line in Figures 4a and 4b corresponds to the magnitude of the electrostatic potential drop, and the differential number flux for energies greater than that magnitude were used in the LM fitting routine. The key result is $\kappa < 10$ for the interval 09:54:06–09:54:19 UT in the equatorward portion of the quasi-stable arc crossing.

detector show a smooth transition from the quasi-trapped ionospheric flux to the accelerated flux [*Evans*, 1974; *Fridman and Lemaire*, 1980; *Pulliam et al.*, 1981].

The model differential number flux below the magnitude of the electrostatic potential drop is somewhat underestimated in magnitude but tracks with the observed differential number flux. At energies near 200 eV, there is a sharp increase in the observed electron flux relative to the model predictions. By fitting the data to the model using a multiplicative factor, we find that a factor of ≈ 1.7 brings the model into good agreement with the data.

The quasi-trapped electron population caused by the Maxwellian distribution is slightly higher than that caused by the kappa distribution. The quasi-trapped electron flux is directly regulated by the magnitude of the precipitating electron flux (especially for the first "bounce" of electrons). If the width of the Maxwellian distribution near the peak flux is broader than the width of the kappa distribution, the magnitude of the quasi-trapped flux can be enhanced, in spite of the rapid exponential decay of the Maxwellian distribution.

Figures 4 and 5 are the results from the fitting routine for the quasi-stable and westward moving auroral crossings, respectively. These figures are formatted similarly. In both figures, panel (a) is a spectrogram of the differential number flux observed by ACES Low for the 15° pitch angle bin. Panel (b) is the result using the kappa distribution function for the 15° pitch angle fit to the data plotted in the same format as panel (a), and including the quasi-trapped ionospheric contribution. The black lines in panels (a) and (b) correspond

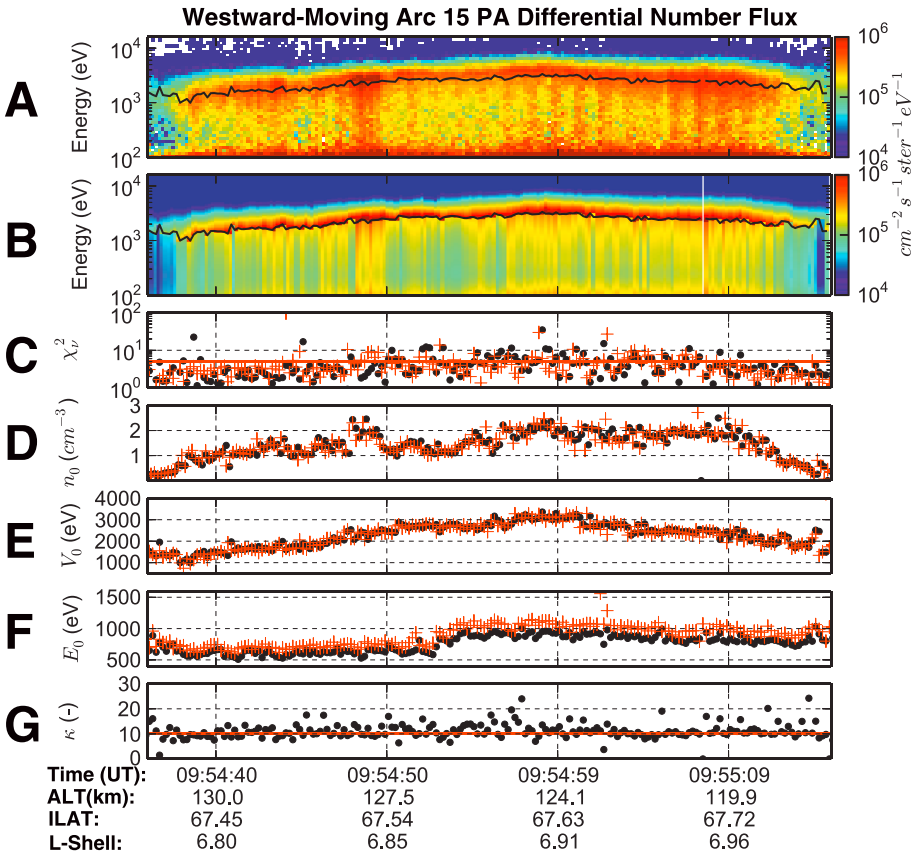

Figure 5. The differential number flux and parameter estimates for the westward moving auroral region, presented in the same format as Figure 4. As can be seen in Figures 5d–5f, the parameter estimates between the kappa distribution and Maxwellian distribution are very similar. Figure 5g shows that $\kappa \approx 10$, which suggests that kappa was not a significant parameter in the fit. Figure 5f shows an upward shift in the thermal energy near 09:54:52 UT.

to the magnitude of the electrostatic potential drop determined from the fitting routine. For brevity, only the pitch angle centered at 15° is shown, although similar results were produced for the 30° pitch angle bin. White intervals in panel (b) indicate regions where the fitting routine did not converge on a solution; no data are available. Panels (c)–(g) show χ^2_ν (reduced χ^2) of the model fit, along with estimates of n_0, Φ_0, E_κ, and κ, respectively. The black dots correspond to using the kappa distribution function, and the red crosses correspond to using a Maxwellian distribution function, noting that κ is irrelevant for a Maxwellian distribution. In Figures 4c and 5c, a red line is set to the value of $\chi^2_\nu = 5$ to guide the eye. Panel (g) has a red horizontal line to denote $\kappa = 10$. Time and ephemeris data are provided for the ACES Low payload along the *x* axis of the figures.

In panels (a) and (b) of Figures 4 and 5, the model reproduces the differential number flux at energies above the magnitude of the potential drop, indicated by the black line in the spectrograms. The width of the differential number flux is broader over the region where kappa values are lowest. Features in the electron flux that persist over multiple time intervals are also reproduced well by the model. For example, a plateau in the electron flux in Figure 4a at 09:54:11 UT is reproduced by the model results in Figure 4b. Flux features mimicking small-scale inverted Vs are embedded within the larger precipitation structure, such as between 09:54:24 and 09:54:28 UT in Figure 4a, are also well reproduced by the model in Figure 4b.

The model flux at energies less than the potential drop has a similar magnitude to that observed by ACES Low; however, the model does not reproduce the magnitude of stripes of intense precipitation, such as after 09:54:59 in Figure 5. The width of the differential number flux near the peak can be truncated and at times appears to be half the width (in energy) of the flux observed by ACES Low. This effect is more pronounced in the differential energy flux ($\rho(E,\alpha) = EJ(E,\alpha)$), which is not shown. This effect is caused by the discontinuity

Table 1. Summary of the Mean and Median Parameter Estimates for the Quasi-Stable and Westward Moving Arc[a]

Time (UT)	Arc	n_0	E_κ	κ	% κ	% Maxwellian
09:54:06–09:54:14	QS	1.6 (1.6) ± 0.04	890 (880) ± 18.	4.0 (3.5) ± 0.3	100	0
09:54:14–09:54:19	QS	1.5 (1.6) ± 0.05	980 (1000)± 25.	6.4 (6.3) ± 0.6	88	12
09:54:19–09:54:28	QS	1.4 (1.4) ± 0.07	970 (980) ± 13.	10. (10.) ± 0.4	56	44
09:54:38–09:54:53	W	1.3 (1.2) ± 0.04	620 (620) ± 6.4	11. (10.) ± 0.2	64	36
09:54:53–09:55:12	W	1.7 (1.8) ± 0.04	870 (870) ± 6.5	11. (11.) ± 0.3	47	53

[a]The columns specify the following: Time in UT, whether the averages were over the quasi-stable (QS) or westward moving arc (W), the source number density, thermal temperature, kappa index, percentage of fit by kappa distribution over the time interval, and percentage of fits by Maxwellian distribution over the time interval. Parameters are recorded as mean (median) ± standard deviation.

in the differential number flux between the quasi-trapped and the accelerated primary electrons. It was found that for the quasi-stable arc, the model and data differed by a factor of $\approx$ 1.5, and for the westward moving aurora, the difference was ≈1.7. On average, the modeled ionospheric portion of the electron flux was within a factor of 2 of the observed electron flux for energies less than the potential drop.

Figure 4g shows the key result of this paper: the value of kappa was significantly less than 10 for the time interval 09:54:06–09:54:17 UT, corresponding to the equatorward entry of ACES Low into the quasi-stable arc. A subdivision is made between the region corresponding to the time interval 09:54:06–09:54:15 UT and 09:54:15–09:54:17 UT. In the first period, the value of kappa is low and fairly constant, and in the second period, there is a transition in kappa from low to high values. In the time interval 09:54:06–09:54:14 UT, kappa had a mean value of 3.9, a median value of 3.5, and a standard deviation of 0.3 (this is recorded as 3.9 (3.5) ± 0.3 in Table 1). The value of kappa increases linearly between 09:54:14 and 09:54:19 UT, with a higher mean and median, and a larger standard deviation of 6.4 (6.3) ± 0.6. The transition in kappa occurs near 09:54:15 UT, when the quasi-stable arc began to precipitously diminish in visible intensity, as shown in Figure 1b. From 09:54:19–09:54:28 UT, the value of kappa remained approximately constant as the payload exited the rapidly diminishing visual arc. Within the last half of the arc, the mean value of kappa was 10. (9.7) ± 0.4, which was very near the initial parameter estimate of $\kappa = 10$. These results suggest that for the first half of the quasi-stable arc, the electron distribution was better fit by a kappa distribution function. The increase in the parameter κ suggests that the source electron distribution became more Maxwellian after approximately 09:54:19 UT, in the second half of the quasi-stable arc. The electron temperature, E_κ, was 900 (880) ± 18., 980 (1000) ± 25., and 970 (980) ± 13., for the lowest-kappa, transitioning-kappa, and constant kappa regions, respectively. The entry of ACES Low into the quasi-stable arc was at an L shell of 6.59 and at 09:54:28, when the payload exited the arc at $L = 6.72$. The transition in the value of kappa occurred at $L = 6.67$, approximately midway through the quasi-stable arc crossing. This L shell maps to approximately geosynchronous orbits in the equatorial plane. ACES Low reached its apogee altitude of 132.6 km during this arc crossing, which was well within the *E* region ionosphere.

Figure 5 shows the precipitating differential number flux for the westward moving auroral region that ACES Low entered at approximately 09:54:38 UT and exited at 09:55:12 UT. For the majority of the westward moving auroral region, the differential number flux is fit almost equally well by a high-value kappa distribution ($\kappa \geq 10$) as by a Maxwellian distribution function. The value of kappa remains relatively constant through the arc, with a mean value of 11 ± 0.2 averaged over the whole westward moving auroral region. An abrupt increase in temperature occurs at 09:54:52 UT, as shown in Figure 5f. Using this change in temperature as a subdivision, the mean temperature from 09:54:38 to 09:54:53 UT was 620 ± 6.4, and for the later portion of the arc, from 09:54:53 to 09:55:12 UT, the mean temperature increased to 870 ± 6.0. Such an increase in temperature is also present in fits of the Maxwellian distribution function. This latter interval with the higher temperature is also correlated with increased number density. From Figure 5, between 09:54:38 and 09:54:53 UT, the number density has a lower average value, but begins to increase following an increase in the electron temperature at 09:54:53 UT. The electrostatic potential drop remains unaffected even though the electron temperature and number density change significantly. All-sky images from this time interval do not indicate any significant brightening in the auroral form. The ACES payload appears to be passing through a westward extension from the larger westward moving auroral form, which has less visual

magnitude relative to the center of the westward moving region. The change in temperature, coupled with the nature of the electron number density, suggest that the ACES payload may have passed through two localized regions: a region that was cooler with a lower electron number density and a region of higher temperature and higher number density.

Table 1 summarizes the mean, median, and standard deviation of the parameter estimates from the fits for both the quasi-stable arc crossing and the westward moving auroral region. The last two columns of Table 1 show the occurrence percentage of using either a kappa distribution or a Maxwellian distribution that produce the lowest value of χ_ν^2. For the interval 09:54:06–09:54:19 UT, which corresponds to the region where $\kappa < 10$ in the quasi-stable arc, the kappa distribution produces a lower value of χ_ν^2 for 95% of the fits. For the interval 09:54:19–09:54:28 UT and the whole westward traveling arc, the percentage of kappa distributions producing a lower χ_ν^2 is 45% versus 55% for Maxwellian distributions. In Figure 5f, the E_0 estimation for the Maxwellian is slightly higher but tracks very well with the E_κ parameter for the kappa distribution. The difference in the temperature estimates between the kappa and Maxwellian distribution is likely due to the additional parameter κ in the fitting routine. Since κ assists in fitting the thermal spread and decay of the distribution, a lower value of temperature and kappa is effectively equivalent to a slightly higher temperature estimate using a Maxwellian distribution. Within the second half of the quasi-stable arc and the westward moving region, the κ distribution does a marginally better job fitting the observed electron flux.

There are two additional notable features in Figures 4 and 5. First, localized precipitation enhancements within the differential number flux are reproduced by the model. Examples of these enhancements are at 09:54:22 UT and 09:54:49 UT in Figure 4 and in the region preceding 09:55:09 UT in Figure 5. These enhanced fluxes correspond to sharp increases in the source electron number density, while the potential drop remains unchanged (aside from an upward or downward gradient over the whole auroral region). This suggests that these regions are associated with localized enhancements in the source electron number density. However, some caution needs to be exercised in this interpretation of these data. Considering that Φ_0 was relatively fixed, the fitting routine may have varied n_0 significantly, so it could appear as a localized enhancement in response to a relatively unchanged electrostatic potential drop.

The second feature is the sharp gradients observed in the differential number flux and gradients in the source electron number density corresponding to the edges of the auroral features. For the quasi-stable arc, in Figure 4d, within a 4 s interval, the number density dropped from 1.5 to 0.4 cm^{-3}. Assuming a nominal payload track velocity of 1 km/s, the density gradient has a horizontal distance of 4 km. As can be seen in Figure 4a, the differential number flux had a nearly step function decrease in flux. This may have corresponded to the rapid weakening of the visible quasi-stable arc. For the westward moving aurora, a similar situation is seen in Figures 5a and 5b. Again, a gradient in the source number density correlates well with the edge of the step-like change in the differential number flux. Another possible explanation for this sharp gradient is that the payload was below the "stopping altitude" of the flux at a few keV [*Kaeppler et al.*, 2012]. This could account for an abrupt change in the observed electron flux, since the electrons would have experienced enough collisions to become effectively indistinguishable from the background electron population. In both cases, gradients in conductivity near the edges of the auroral arc, which are controlled by particle precipitation, have an important role in allowing for horizontal and field-aligned currents to flow.

5. Discussion

5.1. Uncertainty of Parameter Estimates

The χ_ν^2 estimates that result from the fitting routine shown in Figures 4 and 5 have values well above unity, which would be considered to be a "moderately good" fit [*Press et al.*, 2007]. This is especially noticeable for the time interval of the quasi-stable arc crossing, where the parameters are better fit by a kappa distribution. For the equatorward crossing of the quasi-stable arc, there are features within the differential number flux not well reproduced by the model, although the overall character of the electron flux is fit by the model. For example, the electron spectrum at 09:54:08 UT is shown in Figure 6 and is plotted in a similar fashion to Figure 3. Between approximately 4and 6 keV, there is a departure in the form of a "bump" in the observed electron spectrum, as shown in the data. This feature is present in both the 15° and 30° pitch angle bins corresponding to Figures 3 (left) and 3 (right), respectively. It is clear that for the accelerated electron flux, the model captures the character of the differential number flux. However, the model does not reproduce all

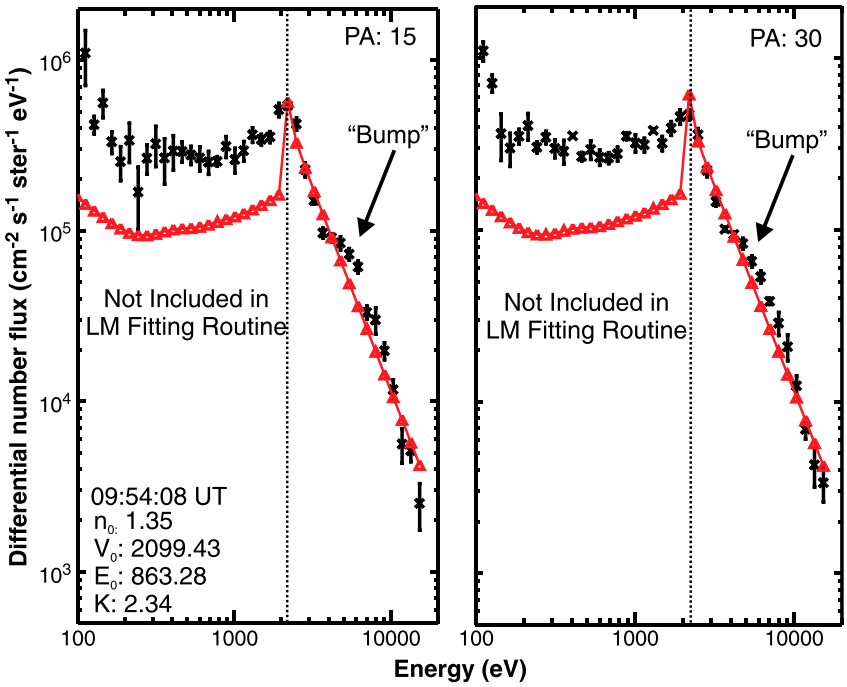

Figure 6. An example of the fit of a kappa distribution showing a departure in the differential number flux as a "bump," which caused an increase in the value of χ_ν^2. The figure shows the (left) 15° and (right) 30° pitch angles. This figure has a similar format as Figure 3. The model using the kappa distribution function fits the overall character of the differential number flux, even if it does not account for all of the features, such as the "bump."

of these departures, such as this "bump" in the differential number flux. As a consequence, the value of χ_ν^2 is larger. These departures were found between 09:54:06 and 09:54:19 UT and correspond to approximately 18% of the data in this time interval. However, it is unclear whether these departures were an instrumental effect or if there was a physical mechanism (such as a plasma instability) that causes these departures. A deeper investigation of the cause of these departures in the differential number flux is outside of the scope of this work.

A routine was devised to quantify the uncertainty of the parameter estimates as a result of uncertainties in the differential number flux. A Monte Carlo technique was used to generate synthetic data from the fit parameters [*Bevington and Robinson*, 2003; *Press et al.*, 2007, section 15.6]. It is assumed that the parameter estimates from the fit are the true parameters that characterize the differential number flux. For the realization of the model using the true parameters [$J(E, \alpha, t)$], a Gaussian random number was applied to the standard error from the observed differential number flux observations and summed with the model differential number flux to produce synthetic data,

$$J_j(E, \alpha, t) = J(E, \alpha, t) + \sigma(t) R_G \tag{10}$$

where $\alpha = 15°$ or 30°, $\sigma(t) = \sigma/\sqrt{5}$ is the standard error on the data over the 192 ms interval, R_G corresponds to a Gaussian random number, j is the index of the instance in the Monte Carlo simulation, and t corresponds to the time interval of interest. The initial guess parameters, n_0, Φ_0, B_0, and E_κ remain fixed through the loop over j instances; however, κ is drawn from a random uniform distribution between values of 1.5 and 35, where the upper limit was imposed to obtain numerically finite values. This was done to test κ explicitly. The fitting routine is run on the synthetic data, $J_j(E, \alpha, t)$, and this process is repeated to produce 200 realizations.

The results from the Monte Carlo simulation were normalized to produce a probability distribution. We expect that the parameters should be represented as Gaussian random variables; however, a tail in the probability distribution may exist if a parameter is particularly insensitive in the fitting routine. We report the 90% confidence interval for the parameters, where the percentage is determined numerically by integrating

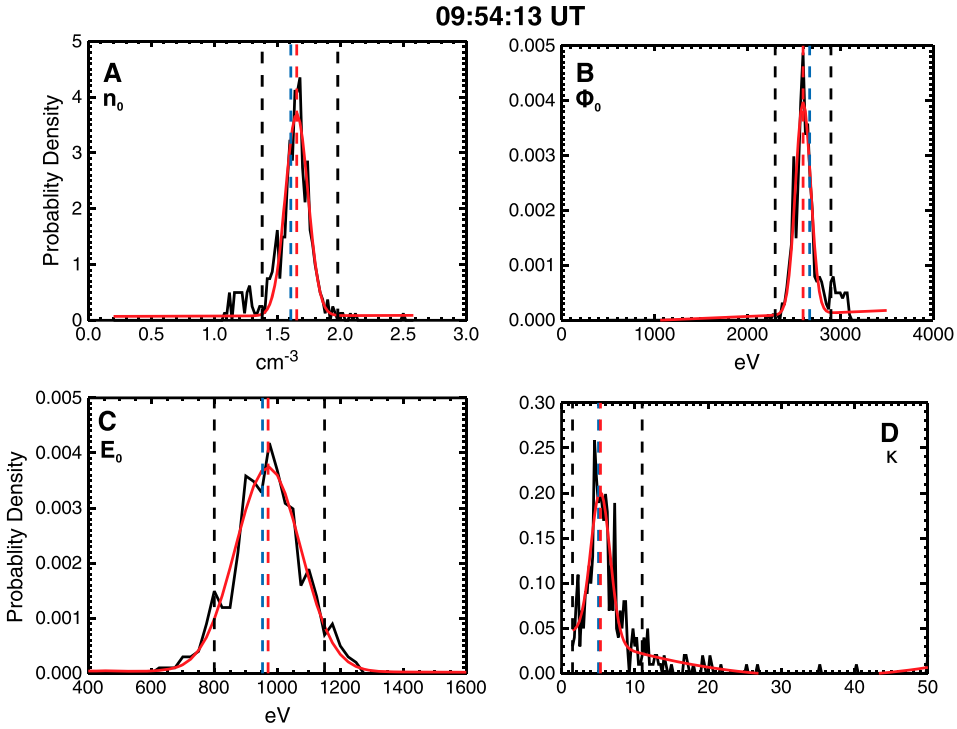

Figure 7. An example of the results from the Monte Carlo simulation quantifying the uncertainties in parameter estimates at 09:54:13 UT, corresponding to the same time interval as Figure 3. The black curve corresponds to the normalized probability distribution. The red curve is a Gaussian fit, including linear and quadratic terms, to account for tails in the probability distribution. The vertical blue dashed line is the parameter estimate from the fitting routine, and the red vertical line is the most probable value determined from the Gaussian fit. The black vertical lines correspond to the 90% confidence interval of the normalized probability distribution. Parameters shown are as follows: (a) source electron density, (b) electrostatic potential drop, (c) source electron temperature, and (d) κ index.

the area under the normalized probability distribution by increasing the interval size about the most probable value.

Figure 7 shows an example of this Monte Carlo calculation at 09:54:13 UT (at the same time as Figure 3 above). Figures 7a–7d show the normalized probability distributions of parameters n_0, Φ_0, E_0, and κ in black, respectively. The red line overplotted is a Gaussian fit, and the dashed blue line corresponds to the true parameter values; that is, the original fit. Ideally these two dashed lines should lie on top of each other. The vertical black dashed lines correspond to the 90% confidence intervals. If a Gaussian is in fact a good fit of these data, then the 90% intervals and 1.645 σ should be equal, where σ is determined from the Gaussian fit. Figure 7d shows a contribution from the tail of the normalized probability distribution for the parameter κ and that the 90% probability interval corresponds to parameter $1.50 \leq \kappa \leq 11.00$. The other parameters in this case are fit by a Gaussian distribution.

Figure 8 shows the results of running the Monte Carlo simulation on the parameter uncertainties for both the quasi-stable arc and the westward moving auroral region, focusing on the parameter κ. The top panel is the model differential number flux for the 15° pitch angle bin, plotted similarly to Figure 4b. Figure 8 (bottom) shows the parameter κ, with the black dot corresponding to the true value (original fit parameter) and the red error bars corresponding to the 90% confidence interval. There is a weak inverted V between the quasi-stable and westward moving auroral region; however, this region was not included in this study. Figure 8, between 09:54:06 and 09:54:16 UT, shows the confidence interval had values of $\kappa \lesssim 10$. After 09:54:16 UT, the confidence interval for kappa has a significantly larger range associated with it, with $\kappa > 10$. This suggests that the kappa parameter is insensitive in the fitting routine after 09:54:16 UT. For the interval from 09:56:06 to 09:54:16 UT, the fitting routine repeatedly finds the kappa distribution function to be a superior fit versus the Maxwellian distribution function and that the fits are sensitive to the parameter κ.

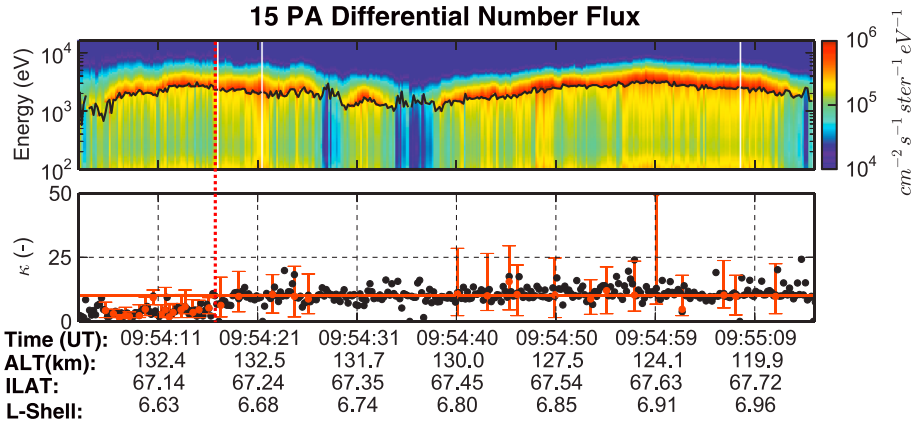

Figure 8. (top) The differential number flux from the fitting routine for the pitch angle centered at 15°. (bottom) The value of kappa with error bars that correspond to the 90% confidence interval. The horizontal red line in Figure 8 (bottom) corresponds to $\kappa = 10$, and the vertical dashed red line corresponds to the transition time from fits by kappa distribution function to fits by the Maxwellian distribution function. The equatorward entry into the first, quasi-stable arc, the values of κ, and their associated uncertainties are generally $\kappa \lesssim 10$. For the latter half of the quasi-stable arc and the westward moving arc, the values of $\kappa \gg 10$, which suggest that the parameter κ is insensitive in the fitting routine.

5.2. Auroral Source Region

We compare our findings with previous observations from rockets and satellites to determine whether the derived parameters are consistent with these observations and to make inferences regarding the source region of the auroral electrons for this event. Before discussing these parameters further, a few limitations must be examined. Based on the value of B_0 that was chosen, the region of the magnetosphere to which these observations map is just above the electrostatic potential drop at 0.8 R_E. Therefore, to infer the properties in the more distant portion of the tail, we assumed that the isotropic plasma observed just above the electrostatic potential drop is representative of the plasma observed along the closed magnetic flux tubes from the more distant region of the tail. This assumption is justified by Liouville's theorem, since the plasma along the flux tube is, to good approximation, collisionless. For simplicity, we use the L shell to determine the location to which the flux tube maps to in the equatorial plane, although it is acknowledged that in active times, the tail can be significantly stretched. The stretched tail configuration may be more consistent with the ACES observations. Second, in the linear regime, the current-voltage relation becomes effectively independent of the parameter B_0. This suggests an ambiguity in the altitude of the source region.

The sounding rocket studies by *Bruening and Goertz* [1986], *Kletzing et al.* [1996], and *Ogasawara et al.* [2006] are most appropriate for comparison with the results from ACES. These missions had payloads that flew directly through discrete aurora. *Bruening and Goertz* [1986] are especially relevant considering that the altitude of the electrostatic potential drop is inferred to be between 2500 and 5000 km, which is very consistent with our assumption that $B_0 = 6$. *Bruening and Goertz* [1986] observed a decrease in the magnitude of the potential drop from 7 keV to 2.5 keV, coupled with an increase in the source electron number density from 0.6 to 1.35 cm^{-3} over the first portion of a discrete arc crossing. In the latter half of the arc crossing, there is an increase in the electrostatic potential drop increases to 4 keV, with a nearly constant source electron density of 0.8 cm^{-3}. The parallel number flux into the ionosphere does not vary by more than a factor of 2 over the arc crossing, even though the number density and potential drop vary significantly [*Bruening and Goertz*, 1986]. *Kletzing et al.* [1996] showed a similar inverse relationship; the magnitude of the potential drop did not exceed 1 keV, and the electron density had magnitudes between 0.5 and 12 cm^{-3}. The results from *Kletzing et al.* [1996] were associated with discrete aurora over the polar cap, and the authors note that the parameters describing the precipitating electrons were lower than what is typically found in the auroral oval region. Our results find an inverse relationship between n_0 and Φ_0, and magnitudes for these parameters that were similar to previous studies.

Our observations show that the source electron temperature ranges between 600 eV and 1100 eV over both auroral crossings. In *Bruening and Goertz* [1986], the electron temperature shows a decreasing character that tracks with the magnitude of the electrostatic potential drop; the magnitude dropped from 3 keV to

1 keV as the payload traversed a visible auroral arc. *Kletzing et al.* [1996] generally inferred a significantly colder population with values between 10 and 200 eV, which could be attributed to the polar cap source region. The results by *Ogasawara et al.* [2006] suggest a source temperature between 270 eV and 720 eV for the kappa distribution function that fits the auroral electron spectrum (using a nonaccelerated kappa distribution function).

We now shift focus to relevant satellite measurements of precipitating electrons over the auroral zone and in situ observations of plasma sheet electrons to compare our parameter estimates. *Shiokawa and Fukunishi* [1991] and *Shiokawa et al.* [2000] fit an accelerated Maxwellian distribution to the electron spectra observed by the F6 and F7 DMSP satellites for two intervals in 1985, which corresponded to active and quiet times. *Shiokawa and Fukunishi* [1991] found that the majority of events near 24:00 MLT corresponded to electrostatic potential drops > 2000 eV and also correlated well with events having column emissions at 5577 Åwith magnitudes > 1 kR (significant enough to produce visible aurora) for both quiet time and active time auroral zone crossings. These events were also found to be centered near 70° invariant latitude, with many of the more active regions showing larger potential drop magnitudes that extended to lower invariant latitudes than was observed for other MLT sectors. Thus, the magnitude of the potential drop derived from DMSP observations and at lower invariant latitudes are consistent with the observations made by ACES. *Shiokawa and Fukunishi* [1991] also showed that the region with the majority of the arc crossings have temperatures > 1000 eV occurred in the 24:00 MLT sector. Moreover, it was found that for quiet and active time arc crossings in this MLT sector, the typical source electron temperatures ranged between 500 and 1000 eV.

Temperature results from the satellite study by *Kletzing et al.* [2003] are in good agreement with our results with respect to both location and time. The equatorward boundary invariant latitudes were consistent with invariant latitudes traversed by ACES. The median 15 min averages of temperature corresponding to an equatorward boundary crossing near the 24:00 MLT sector and the invariant latitude around 67° had values of $E_0 \approx$1000 eV, respectively. The electron temperature observed on ACES was approximately 1000 eV for the quasi-stable, and for the westward moving aurora, the temperature was 600 eV and 1000 eV for the equatorward and poleward sides of that crossing, respectively.

The source electron density is the parameter that exhibits the most variation between our observations and previous satellite results. *Shiokawa and Fukunishi* [1991] report that the dominant number density for both active and quiet time arcs appears to be < 1.5 cm^{-3}. However, observations within the midnight MLT sector indicate isolated instances of number densities > 1.5 cm^{-3}, and some of these events also have simultaneous potential drop magnitudes > 2000 eV. For the studies reviewed by *Olsson et al.* [1998], the inferred number density typically ranges from 0.05 to 0.6 cm^{-3}, with an isolated instance of 2 cm^{-3} [*Bruning et al.*, 1990]. The results by *Kletzing et al.* [2003] show remarkable contrast with our number densities. For similar regions in MLT and invariant latitudes (similar to the temperature results above), the median 15 min average number density reported on the equatorward side was 0.4 cm^{-3}. This is approximately a factor of 2–3 smaller than the ACES observations. It was noted that 80% of the events sampled corresponded to quiet time conditions with $K_p \leq 2$. This sampling, biased toward more quiet conditions, may have resulted in lower values of the number density.

Two other satellite studies suggest that values of n_0 are nearer to the observations of ACES. *Borovsky et al.* [1998] used the 1989-046 satellite near geosynchronous orbit to demonstrate the homogeneity of the plasma sheet as a function of time. For 84 passes near magnetic midnight, an average ion plasma sheet density near 1 cm^{-3} was found. As shown in the ephemeris data in Figures 4 and 5, the L shell that was traversed by ACES maps to approximately geosynchronous orbit in the equatorial plane. *Wing and Newell* [1998] mapped DMSP data from 800 km back into the plasma sheet. Fitting the electron spectra on DMSP allowed typical values to be calculated for the ion plasma sheet pressure, temperature, and number density. Ion plasma sheet densities were higher in the near-Earth regions ($\approx 10R_e$) than in the tail, with near-Earth values near 1 cm^{-3}. If quasi-neutrality is assumed, the number densities observed by ACES appear to be more consistent with observations of the near-Earth plasma sheet.

The values of κ that were observed by ACES Low are in good agreement with previous observations. Our observations show that $\kappa = 2 - 8$ within the equatorward portion of the quasi-stable arc. The values of κ are in good agreement with the results from *Kletzing et al.* [2003], who found that the electrons were best fit by a $\kappa \leq 10$ and FREJA observations of $\kappa = 4 - 7$ by *Olsson and Janhunen* [1998]. Our observations of κ were also consistent with the sounding rocket observations by *Ogasawara et al.* [2006] who found that $\kappa \approx 8$.

The detectors flown in *Ogasawara et al.* [2006] had increased energy range, allowing for a greater ability to resolve the high-energy tail of the kappa distribution.

To summarize, the parameter estimates determined from the model fit to the in situ differential number flux are consistent with previous observations that have inferred or measured similar plasma sheet quantities. Our observations are in good agreement with previous sounding rocket results for the source density, temperature, and inferred altitude of the potential drop. The electron temperature and kappa are in good agreement with in situ observations in the high-latitude plasma sheet by *Kletzing et al.* [2003]. Our observations of the plasma sheet electron density show more variation relative to previous satellite and rocket observations. If quasi-neutrality is assumed, our plasma sheet density measurements are within a factor of 2 of the near-Earth values based on the observations by *Borovsky et al.* [1998] and *Wing and Newell* [1998] and a factor of 2–4 with the equatorward boundary observations made by *Kletzing et al.* [2003].

These results from the ACES Low sounding rocket are consistent with the results of *Kletzing et al.* [2003], that the high-latitude plasma sheet electron population is characterized by a kappa distribution function and forms the source region of auroral electrons. *Kletzing et al.* [2003] took the approach that the source region mapped down to invariant latitudes consistent with the auroral oval. Our observations add to those previous results by showing that, near the ionospheric foot point, field-aligned electrons are fit by a kappa distribution function and correlate directly to the equatorward side of a discrete, quasi-stable auroral arc. The source electron region that was observed by the ACES Low payload has electron density signatures consistent with the near-Earth plasma sheet. The high-energy tail associated with a kappa distribution function is a signature that is consistent with other observations in the plasma sheet. The observations made by the ACES Low payload are among a few observations of kappa distribution functions at *E* region altitudes.

5.3. Quasi-Trapped Electron Flux

The contribution from the quasi-trapped electron population was somewhat underestimated in the precipitation model. A few possible sources of uncertainty may explain this difference in magnitude, especially the model that describes the scattering and ionizing processes [*Banks et al.*, 1974]. *Evans* [1974] used Figure 7 in *Banks et al.* [1974] to describe the upward directed flux that is generated by a 10 keV monoenergetic beam, which precipitates isotropically back onto the ionosphere if the parallel energy is not large enough to overcome the potential drop. However, the upward directed flux was determined at three altitudes: 200 km, 125 km, and 105 km [*Banks et al.*, 1974]. Based on an examination of Figures 2 and 3 from *Evans* [1974], it is presumed that the upward flux at 200 km altitude was divided at 500 eV to create Figure 2 for the secondary electron response ($E < 500$ eV) and Figure 3 for the degraded primary ($E > 500$ eV) response in *Evans* [1974], respectively. The upward flux predicted in the *Banks et al.* [1974] model for an altitude of 125 km is more consistent with the altitude that was traversed by ACES Low. Between 200 eV and 7 keV, there is a 34% (maximum) increase in the upward directed flux for the 125 km model versus the 200 km model. It would be expected that the secondary and degraded primary responses would increase by 34% over that energy range. This enhancement would provide better agreement between the observed electron flux and the model.

The neutral atmosphere used in this model is another possible source of uncertainty that may impact the response of secondary electrons or degraded primaries. The neutral atmosphere number density of the dominant species forms the field of scatters that the precipitating electrons encounter. However, *Banks et al.* [1974] argue that electrons with energies < 500 eV, to first order, the effect of the neutral atmosphere can be neglected, but the neutral density for $E > 500eV$ is linear in the response. The neutral atmosphere model used by *Banks et al.* [1974] was the 1000° K thermosphere model in *Banks and Kockarts* [1973]. For comparison, an instance of the NRLMSIS00 model was run at the approximate apogee location of the ACES payload [*Picone et al.*, 2002]. For the dominant neutral density *O*, the MSIS density was approximately a factor of 2 less than the 1000°K model, especially at lower altitudes. On the other hand, there was very good agreement between MSIS and the 1000°K model for the N_2 species, the other dominant species. This suggests that for the ACES mission, the secondary response and the degraded primary response may have been overestimated and may be reduced if the NRLMSIS00 model is used instead of the 1000°K model.

Finally, the general trend of the quasi-trapped electron flux is well represented by the model relative to the observed data. However, near energies of 100–200 eV, a very rapid increase sometimes occurs in the electron flux that may not be represented by the secondary electron response in *Evans* [1974]. This suggests that

some aspect of the generation of secondary electron flux and low-energy degraded primary flux needs to be resolved further but is outside of the scope of this paper.

6. Conclusions

Electrostatic electron detectors flown on the ACES Low payload made observations of precipitating electron spectra that are fit by kappa distribution functions and these electron spectra correlated with two discrete auroral arc crossings. For the equatorward side of the first auroral arc crossing, observations from precipitating auroral electrons for pitch angles centered at 15° and 30° were found to be fit by kappa distribution functions. These observations were made as the payload was entering a relatively stable east-west extended auroral arc termed the quasi-stable arc by *Kaeppler et al.* [2012]. For the poleward side of the first auroral arc crossing and throughout the second auroral arc crossing, the differential number flux was fit by a Maxwellian distribution function. The observations that the precipitating electron spectra at *E* region altitudes is fit by a Maxwellian distribution function provide additional confirmation of previous results. A precipitous fading of the first arc was observed in the all-sky imager data which correlated with a division between the kappa distribution function fit of the electron spectra versus the Maxwellian distribution function fit of the electron spectra.

These observations are among the first to show that kappa distribution functions appropriately describe field-aligned precipitating electrons at *E* region altitudes and expand the previous observations by *Ogasawara et al.* [2006]. These observations are consistent with the results in *Kletzing et al.* [2003], which found that the high-latitude plasma sheet is fit by a kappa distribution function and is the source region of auroral electrons. These results provide direct evidence that kappa distributions retain their character near the ionospheric foot point.

A Monte Carlo simulation was run to quantify the uncertainty in the parameter estimates that resulted from uncertainties in the in situ differential number flux measurements. For the interval 09:54:06–09:54:16 UT, corresponding to the equatorward side of the quasi-stable arc crossing, the 90% confidence interval had values of $\kappa \lesssim 10$. This suggests that the kappa distribution function is a superior fit of the observed electron flux data for this interval in time. However, for the poleward side of the first quasi-stable arc crossing and for the westward moving auroral region, the parameter kappa was insensitive in the fitting routine. The power law character of the kappa distribution could be used as an observational signature to infer the auroral plasma sheet source region.

The model by *Evans* [1974] adequately reproduces the full electron spectra over a discrete auroral arc. The quasi-trapped ionospheric population, which was not included in the Levenberg-Marquardt fitting routine, was within a factor of 2 of the observed differential number flux for both of the auroral crossings. The higher magnitude of the quasi-trapped ionospheric population reduces the magnitude of the discontinuity near the electrostatic potential drop, which signifies the difference between the quasi-trapped flux and the accelerated precipitating flux. This study is one of few that has experimentally tested the *Evans* [1974] model for the quasi-trapped portion of the auroral electrons.

Acknowledgments
This work was supported by the National Science Foundation (NSF) grant AGS-1133009 and NSF EAR-0836152 to SRI International. This work was also supported by NASA grant NNX07AJ97G. We acknowledge NASA contract NAS5-02099 and V. Angelopoulos for use of data from the THEMIS Mission, including, S. Mende and E. Donovan for use of the ASI data, the CSA for logistical support in fielding and data retrieval from the GBO stations, and NSF for support of GIMNAST through grant AGS-1004736. We also thank M. Greffen and E. Spanswick for their assistance in processing the THEMIS ASI data. Data will be made available by contacting the first author.

Larry Kepko thanks Adolfo Viñas and another reviewer for their assistance in evaluating this paper.

References

Albert, R. D., and P. J. Lindstrom (1970), Auroral-particle precipitation and trapping caused by electrostatic double layers in the ionosphere, *Science*, *170*, 1398–1401, doi:10.1126/science.170.3965.1398.

Banks, P. M., and G. Kockarts (1973), *Aeronomy*, Academic Press, New York.

Banks, P. M., C. R. Chappell, and A. F. Nagy (1974), A new model for the interaction of auroral electrons with the atmosphere: Spectral degradation, backscatter, optical emission, and ionization, *J. Geophys. Res.*, *79*, 1459–1470, doi:10.1029/JA079i010p01459.

Baumjohann, W., and R. Treumann (1996), *Basic Space Plasma Physics*, 329 pp., Imperial College Press, London, U. K.

Bennett, E. L., M. Temerin, and F. S. Mozer (1983), The distribution of auroral electrostatic shocks below 8000-km altitude, *J. Geophys. Res.*, *88*, 7107–7120, doi:10.1029/JA088iA09p07107.

Bevington, P., and D. Robinson (2003), *Data Reduction and Error Analysis for the Physical Sciences*, McGraw-Hill Higher Education, McGraw-Hill, Boston, Mass.

Borovsky, J. E. (1993), Auroral arc thicknesses as predicted by various theories, *J. Geophys. Res.*, *98*, 6101–6138, doi:10.1029/92JA02242.

Borovsky, J. E., M. F. Thomsen, R. C. Elphic, T. E. Cayton, and D. J. McComas (1998), The transport of plasma sheet material from the distant tail to geosynchronous orbit, *J. Geophys. Res.*, *103*, 20,297–20,332, doi:10.1029/97JA03144.

Bruening, K., and C. K. Goertz (1986), Dynamics of a discrete auroral arc, *J. Geophys. Res.*, *91*, 7057–7064, doi:10.1029/JA091iA06p07057.

Bruning, K., L. P. Block, G. T. Marklund, L. Eliasson, and R. Pottelette (1990), Viking observations above a postnoon aurora, *J. Geophys. Res.*, *95*, 6039–6049, doi:10.1029/JA095iA05p06039.

Burch, J. L., S. A. Fields, W. B. Hanson, R. A. Heelis, R. A. Hoffman, and R. W. Janetzke (1976), Characteristics of auroral electron acceleration regions observed by atmosphere explorer C, *J. Geophys. Res.*, *81*, 2223–2230, doi:10.1029/JA081i013p02223.

Chiu, Y. T., and M. Schulz (1978), Self-consistent particle and parallel electrostatic field distributions in the magnetospheric-ionospheric auroral region, *J. Geophys. Res.*, *83*, 629–642, doi:10.1029/JA083iA02p00629.
Christon, S. P., D. G. Mitchell, D. J. Williams, L. A. Frank, C. Y. Huang, and T. E. Eastman (1988), Energy spectra of plasma sheet ions and electrons from about 50 eV/e to about 1 MeV during plamsa temperature transitions, *J. Geophys. Res.*, *93*, 2562–2572, doi:10.1029/JA093iA04p02562.
Christon, S. P., D. J. Williams, D. G. Mitchell, L. A. Frank, and C. Y. Huang (1989), Spectral characteristics of plasma sheet ion and electron populations during undisturbed geomagnetic conditions, *J. Geophys. Res.*, *94*, 13,409–13,424, doi:10.1029/JA094iA10p13409.
Christon, S. P., D. J. Williams, D. G. Mitchell, C. Y. Huang, and L. A. Frank (1991), Spectral characteristics of plasma sheet ion and electron populations during disturbed geomagnetic conditions, *J. Geophys. Res.*, *96*, 1–22, doi:10.1029/90JA01633.
Dors, E. E., and C. A. Kletzing (1999), Effects of suprathermal tails on auroral electrodynamics, *J. Geophys. Res.*, *104*, 6783–6796, doi:10.1029/1998JA900135.
Elphic, R. C., et al. (1998), The auroral current circuit and field-aligned currents observed by FAST, *Geophys. Res. Lett.*, *25*, 2033–2036, doi:10.1029/98GL01158.
Evans, D. S. (1974), Precipitating electron fluxes formed by a magnetic field aligned potential difference, *J. Geophys. Res.*, *79*, 2853–2858, doi:10.1029/JA079i019p02853.
Feldshtein, I. I., and I. I. Galperin (1985), The auroral luminosity structure in the high-latitude upper atmosphere—Its dynamics and relationship to the large-scale structure of the Earth's magnetosphere, *Rev. Geophys.*, *23*, 217–275, doi:10.1029/RG023i003p00217.
Frank, L. A., and K. L. Ackerson (1971), Observations of charged particle precipitation into the auroral zone, *J. Geophys. Res.*, *76*, 3612–3643, doi:10.1029/JA076i016p03612.
Fridman, M., and J. Lemaire (1980), Relationship between auroral electrons fluxes and field aligned electric potential difference, *J. Geophys. Res.*, *85*, 664–670, doi:10.1029/JA085iA02p00664.
Goertz, C. K., and R. W. Boswell (1979), Magnetosphere-ionosphere coupling, *J. Geophys. Res.*, *84*, 7239–7246, doi:10.1029/JA084iA12p07239.
Janhunen, P. (1999), On the current-voltage relationship in fluid theory, *Ann. Geophys.*, *17*, 11–26, doi:10.1007/s00585-999-0011-y.
Janhunen, P., and A. Olsson (1998), The current-voltage relationship revisited: Exact and approximate formulas with almost general validity for hot magnetospheric electrons for bi-Maxwellian and kappa distributions, *Ann. Geophys.*, *16*, 292–297, doi:10.1007/s00585-998-0292-6.
Kaeppler, S. R. (2013), A Rocket-borne investigation of auroral electrodynamics within the auroral ionosphere, PhD thesis, Univ. of Iowa.
Kaeppler, S. R., et al. (2012), Current closure in the auroral ionosphere: Results from the auroral current and electrodynamics structure rocket mission, in *Auroral Phenomenology and Magnetospheric Processes: Earth And Other Planets, Geophys. Monogr. Ser.*, vol. 197, edited by A. Keiling et al., pp. 183–192, AGU, Washington, D. C., doi:10.1029/2011GM001177.
Karlsson, T. (2012), The acceleration region of stable auroral arcs, in *Auroral Phenomenology and Magnetospheric Processes: Earth And Other Planets, Geophys. Monogr. Ser.*, vol. 197, edited by A. Keiling et al., pp. 227–239, AGU, Washington, D. C., doi:10.1029/2011GM001179.
Kletzing, C. A. (1994), Electron acceleration by kinetic Alfvén waves, *J. Geophys. Res.*, *99*, 11,095–11,104, doi:10.1029/94JA00345.
Kletzing, C. A., G. Berg, M. C. Kelley, F. Primdahl, and R. B. Torbert (1996), The electrical and precipitation characteristics of morning sector Sun-aligned auroral arcs, *J. Geophys. Res.*, *101*, 17,175–17,190, doi:10.1029/96JA00294.
Kletzing, C. A., J. D. Scudder, E. E. Dors, and C. Curto (2003), Auroral source region: Plasma properties of the high-latitude plasma sheet, *J. Geophys. Res.*, *108*(A10), 1360, doi:10.1029/2002JA009678.
Knight, S. (1973), Parallel electric fields, *Planet. Space Sci.*, *21*, 741–750, doi:10.1016/0032-0633(73)90093-7.
Lemaire, J., and M. Scherer (1973), Plasma sheet particle precipitation: A kinetic model, *Planet. Space Sci.*, *21*, 281–289, doi:10.1016/0032-0633(73)90012-3.
Lemaire, J., and M. Scherer (1974), Ionosphere-plasmasheet field-aligned currents and parallel electric fields, *Planet. Space Sci.*, *22*, 1485–1490, doi:10.1016/0032-0633(74)90013-0.
Livadiotis, G., and D. J. McComas (2013), Understanding kappa distributions: A toolbox for space science and astrophysics, *Space Sci. Rev.*, *175*, 183–214, doi:10.1007/s11214-013-9982-9.
Lu, G., P. H. Reiff, J. L. Burch, and J. D. Winningham (1991), On the auroral current-voltage relationship, *J. Geophys. Res.*, *96*, 3523–3531, doi:10.1029/90JA02462.
Lyons, L. R. (1980), Generation of large-scale regions of auroral currents, electric potentials, and precipitation by the divergence of the convection electric field, *J. Geophys. Res.*, *85*, 17–24, doi:10.1029/JA085iA01p00017.
Lyons, L. R. (1981), Discrete aurora as the direct result of an inferred high-altitude generating potential distribution, *J. Geophys. Res.*, *86*(A1), 1–8, doi:10.1029/JA086iA01p00001.
Lyons, L. R., D. S. Evans, and R. Lundin (1979), An observed relation between magnetic field aligned electric fields and downward electron energy fluxes in the vicinity of auroral forms, *J. Geophys. Res.*, *84*, 457–461, doi:10.1029/JA084iA02p00457.
Mallinckrodt, A. J. (1985), A numerical simulation of auroral ionospheric electrodynamics, *J. Geophys. Res.*, *90*, 409–417, doi:10.1029/JA090iA01p00409.
Newell, P. T., Y. I. Feldstein, Y. I. Galperin, and C.-I. Meng (1996), Morphology of nightside precipitation, *J. Geophys. Res.*, *101*, 10,737–10,748, doi:10.1029/95JA03516.
Ogasawara, K., K. Asamura, T. Takashima, Y. Saito, and T. Mukai (2006), Rocket observation of energetic electrons in the low-altitude auroral ionosphere during the DELTA campaign, *Earth Planet. Space*, *58*, 1155–1163.
Olsson, A., and P. Janhunen (1998), Field-aligned conductance values estimated from Maxwellian and kappa distributions in quiet and disturbed events using Freja electron data, *Ann. Geophys.*, *16*, 298–302, doi:10.1007/s00585-998-0298-0.
Olsson, A., L. Andersson, A. I. Eriksson, J. Clemmons, R. E. Erlandsson, G. Reeves, T. Huges, and J. S. Murphee (1998), Freja studies of the current-voltage relation in substorm-related events, *J. Geophys. Res.*, *103*, 4285–4302, doi:10.1029/97JA00560.
Paschmann, G., S. Haaland, and R. Treumann (2002), Auroral plasma physics, *Space Sci. Rev.*, *103*, 41–92, doi:10.1023/A:1023030716698.
Picone, J. M., A. E. Hedin, D. P. Drob, and A. C. Aikin (2002), NRLMSISE-00 empirical model of the atmosphere: Statistical comparisons and scientific issues, *J. Geophys. Res.*, *107*(A12), SIA 15-1–SIA 15-16, doi:10.1029/2002JA009430.
Pierrard, V. (1996), New model of magnetospheric current-voltage relationship, *J. Geophys. Res.*, *101*, 2669–2676, doi:10.1029/95JA00476.
Press, W., S. Teukolsky, W. Vetterling, and B. Flannery (2007), *Numerical Recipes 3rd Edition: The Art of Scientific Computing*, Cambridge Univ. Press, New York.
Pulliam, D. M., H. R. Anderson, K. Stamnes, and M. H. Rees (1981), Auroral electron acceleration and atmospheric interactions: (1) Rocket-borne observations and (2) scattering calculations, *J. Geophys. Res.*, *86*, 2397–2404, doi:10.1029/JA086iA04p02397.

Reiff, P. H., H. L. Collin, J. D. Craven, J. L. Burch, and J. D. Winningham (1988), Determination of auroral electrostatic potentials using high- and low-altitude particle distributions, *J. Geophys. Res.*, *93*, 7441–7465, doi:10.1029/JA093iA07p07441.

Shiokawa, K., and H. Fukunishi (1991), Global characteristics of field-aligned acceleration processes associated with auroral arcs, *J. Geomagn. Geoelec.*, *43*, 691–719.

Shiokawa, K., H. Fukunishi, H. Yamagishi, H. Miyaoka, and R. Fujii (1990), Rocket observation of the magnetosphere-ionosphere coupling processes in quiet and active arcs, *J. Geophys. Res.*, *95*, 10,679–10,686, doi:10.1029/JA095iA07p10679.

Shiokawa, K., W. Baumjohann, G. Haerendel, and H. Fukunishi (2000), High- and low-altitude observations of adiabatic parameters associated with auroral electron acceleration, *J. Geophys. Res.*, *105*, 2541–2550, doi:10.1029/1999JA900458.

Stasiewicz, K., et al. (2000), Small scale Alfvénic structure in the Aurora, *Space Sci. Rev.*, *92*, 423–533.

Vasyliunas, V. M. (1968), A survey of low-energy electrons in the evening sector of the magnetosphere with OGO 1 and OGO 3, *J. Geophys. Res.*, *73*, 2839–2884, doi:10.1029/JA073i009p02839.

Weimer, D. R., D. A. Gurnett, C. K. Goertz, J. D. Menietti, and J. L. Burch (1987), The current-voltage relationship in auroral current sheets, *J. Geophys. Res.*, *92*, 187–194, doi:10.1029/JA092iA01p00187.

Wing, S., and P. T. Newell (1998), Central plasma sheet ion properties as inferred from ionospheric observations, *J. Geophys. Res.*, *103*, 6785–6800, doi:10.1029/97JA02994.

Winningham, J. D., W. J. Heikkila, F. Yasuhara, and S.-I. Akasofu (1975), The latitudinal morphology of 10-eV to 10-keV electron fluxes during magnetically quiet and disturbed times in the 2100-0300 MLT sector, *J. Geophys. Res.*, *80*, 3148–3171, doi:10.1029/JA080i022p03148.

Winningham, J. D., T. W. Speiser, E. W. Hones Jr., R. A. Jeffries, W. H. Roach, D. S. Evans, and H. C. Stenbaek-Nielsen (1977), Rocket-borne measurements of the dayside cleft plasma—The Tordo experiments, *J. Geophys. Res.*, *82*, 1876–1888, doi:10.1029/JA082i013p01876.